Supplementary Material for

Imaging covalent bond formation by H atom scattering from graphene

Hongyan Jiang, Marvin Kammler, Feizhi Ding, Yvonne Dorenkamp, Frederick R. Manby, Alec. M. Wodtke*, Thomas F. Miller III*, Alexander Kandratsenka*, Oliver Bünermann*

*Corresponding author. Email: oliver.buenermann@chemie.uni-goettingen.de (O.B.); tfm@caltech.edu (T.F.M.); akandra@gwdg.de (A.K.); alec.wodtke@mpibpc.mpg.de (A.M.W.)

Published 26 April 2019, *Science* **364**, 379 (2017)
DOI: 10.1126/science.aaw6378

This PDF file includes:

Other Supplementary Material for this manuscript includes the following:
(available at science.sciencemag.org/content/364/6438/379/suppl/DC1)

S1. Methods

Experimental procedures

The Pt(111) substrate was cleaned by several cycles of Ar^+ ion sputtering (30 mins) followed by annealing at 900°C (30 mins) and then flashing to 1000°C (2 mins). Surface cleanliness and structure were checked by Auger electron spectroscopy (AES) and low energy electron diffraction (LEED). The graphene sample was prepared by dosing ethylene on a clean Pt(111) substrate at 700 ^oC for 15 mins. The ethylene partial pressure was kept at 3×10^{-8} mbar during the dosing. The quality of the single layer graphene was confirmed by AES, LEED (Fig. S1) and by the comparison between scattering results from pristine Pt(111) surface and the graphene sample.

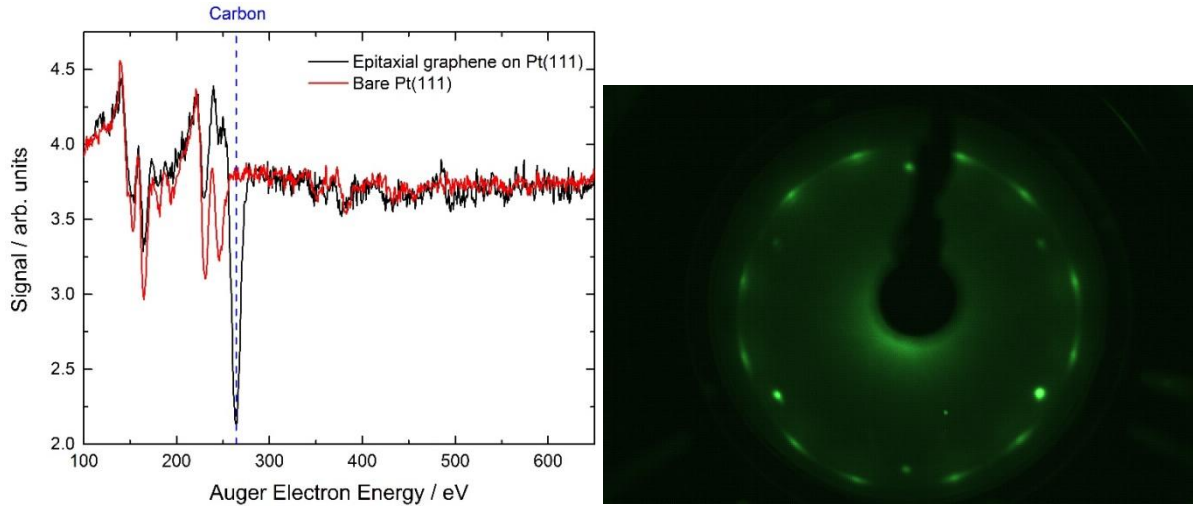

Figure S1: Characterization of graphene sample. (left panel) Auger spectrum of Pt(111) (red) and epitaxial graphene grown on Pt(111). The C Auger electron peak is marked by the blue dashed line. No other elements are detected, indicating the cleanliness of the surfaces. **(right panel) Low energy electron diffraction (LEED) spectrum of epitaxial graphene on Pt(111).** Electron incidence energy is 87 eV. The six circular diffraction spots at smaller polar diffraction angles are from Pt(111); three spots are dim and three bright. At slightly larger polar diffraction angles, twelve spots from graphene can be seen. Each of two orientational domains in the sample gives rise to six spots. The spots are broadened in the azimuthal direction, due to the weak interaction with Pt, which leads to a distribution of graphene Pt orientations with ~ 5˚ width.

The experimental apparatus has been described in detail in Ref. (*36*). Nearly mono-energetic hydrogen atom beams are generated by photolyzing a supersonic beam of hydrogen iodide with ArF or KrF excimer laser light. A small fraction of the atoms pass a skimmer, enter the first of two differential pumping chambers and pass into an ultrahigh vacuum chamber, where the graphene sample is held. The graphene is held on a 6-axis manipulator, allowing variation of the incidence angle, ϑ_I. The scattered H atoms are excited to a long lived Rydberg state by two spatially and temporally overlapped laser pulses passing parallel to the sample at a distance of 0.7 mm. The first laser pulse excites the 1s-2p transition at 121.57 nm and the second excites

the 2p-n=34 transition close to 365 nm. The neutral Rydberg atoms travel 250 mm where they are field ionized and detected by an MCP. The arrival time is recorded using a multi-channel scalar. The rotatable detector allows time-of-flight spectra to be recorded at various scattering angles, ϑ_S. The H-atoms' incidence translational energy, E_I, can be controlled by changing the photolysis wavelength. The normal component of the incidence translational energy can be varied by changing the incidence angle at a constant E_I.

Theoretical methods

General approach: Embedded mean-field theory

Embedded mean-field theory (EMFT) (*17-19*) provides energies and forces from first-principles for parameterization of the REBO potential. EMFT is an electronic structure embedding approach that allows a subset of a system to be described using a relatively more accurate but expensive mean-field theory (such as DFT with a hybrid functional and large basis set), while the remainder of the system is described using a lower accuracy and cheaper mean-field level (such as DFT with a LDA functional and a small basis set). In the EMFT method, the subsystems are partitioned in terms of the atom-centered atomic orbital basis. Unlike the ONIOM method (*37*), EMFT does not require specification of the number of electrons per subsystem, nor does it require specification of the spin-state of the subsystem; only the total number of electrons and the total spin-state of the system is specified. The method is accurate and efficient over a wide range of systems and chemical applications, including those that involve subsystem partitioning across conjugated bonding networks (*17-19*).

General approach: Reactive empirical bond order potential

The second generation reactive empirical bond order potential (REBO) was developed by Brenner *et al.* (*20*) to describe various carbon modifications and hydrocarbons with an accurate, flexible, transferable and computationally efficient analytic potential (*38*). It is based on the ideas of Abell and Tersoff who assumed that the binding energy between two atoms can be modeled by the sum of an attractive and a repulsive term (*39, 40*). The attractive term can either be enhanced or weakened by a bond order factor. While attraction and repulsion is only a function of the distance between two atoms, the bond order term also takes hybridization of the carbon atoms into account. Information about an atoms hybridization is inferred from its surroundings using Abell's argument that the bond order is proportional to the inverse square root of the coordination number. REBO also includes the effects of radical species within a molecular structure as well as rotation about dihedral angles for carbon–carbon double bonds. The interaction range is limited by a cutoff function chosen in such that the nearest neighbors are

always accounted for while the second nearest neighbor are fully excluded. The strength of the interaction is determined by multiple quadratic-, cubic- and higher-order, multi-dimensional spline functions. The default parameter set for standard REBO was tuned to reproduce the potential energy surfaces of solid carbon structures and small organic molecules. Although REBO with its default parameter set has been successfully used for many hydrocarbon configurations, it does not give accurate results for H interactions with graphene. Consequently, we used *ab initio* electronic structure data obtained from EMFT to train the parameter set for accurate results in this system.

Computational details. 1. Benchmarking the electronic structure methods.

The current section compares the results of various electronic structure methods in describing the binding-energy well depth and barrier height for an H atom interacting with graphene, including the CCSD(T), DFT, EMFT, and EMFT-REBO methods. The CCSD(T) results were previously reported (*24*). DFT calculations are performed with a hybrid functional using an atom-centered Gaussian-type orbital (GTO) basis (B3LYP/cc-pVDZ) (*41-45*), as well as with a GGA functional (PBE) (*46*) with Grimme D2 corrections (*47*) using a plane-wave basis with a 400 eV cutoff and *k*-point sampling with a gamma-centered mesh of 8x8x1. EMFT results are obtained with a B3LYP/cc-pVDZ description (*41-45*) for the atoms in the vicinity of the H collision and with an LDA/STO-3G description (*43, 48, 49*) for the remaining atoms (see *Section SI Computational Details 2* for details), and EMFT-REBO results are obtained using the REBO method to fit the EMFT potential energy points (see *Section SI Computational Details 3* for details).

All EMFT and GTO-based DFT calculations reported in this study are performed using the *entos* molecular simulation package (*50*). These calculations employ standard self-consistent field (SCF) procedures, including use of superposition of the atomic densities (SAD) as the initial guess, the direct inversion in the iterative subspace (DIIS) algorithm for SCF acceleration, and a convergence threshold of 10^{-5} a.u. on the maximum value of the orbital gradient. Plane-wave DFT calculations are performed using the VASP software package (*51-54*). For the plane-wave calculations, spin polarization is included, and we employ the tetrahedron method with Blöchl corrections (*55*) to treat partial occupancies with the default smearing parameter of 0.2 eV. Interactions between the core and valence electrons are modeled by the projector augmented wave approach (*55*). The relaxation of the electronic degrees of freedom is stopped when the change in energy between iterations is smaller than 10^{-5} eV. In the calculations of the minimum energy pathway, convergence of the ionic relaxation loop is reached when

all forces are smaller than 10^{-3} eV/Å. The chemisorption well depth and barrier heights are reported in Table S1, and the full MEPs are reported in Figure S2.

Table S1. Calculated chemisorption well depth and barrier height (in eV) for H atom on-top adsorption on graphene at various levels of theory.[a]

Graphene system	Method	Well depth (eV)	Barrier height (eV)
Coronene	CCSD(T)/cc-pVDZ[b]	-0.58	0.37
$C_{42}H_{16}$	B3LYP/cc-pVDZ	-0.80	0.27
	EMFT[c]	-0.59	0.28
Periodic (3 x 4 unit cell)	PBE/plane-wave	-0.84	0.14
Periodic (3 x 4 unit cell)	EMFT-REBO	-0.61	0.26

[a] The energy at dissociation limit is chosen as reference. Zero-point energy corrections are not included. For finite-system calculations, basis set superposition errors are negligible and thus not included.
[b] Ref. (*24*).
[c] High-level : B3LYP/cc-pVDZ; low-level: LDA/STO-3G; Subsystem partitioning shown in Fig. S5.

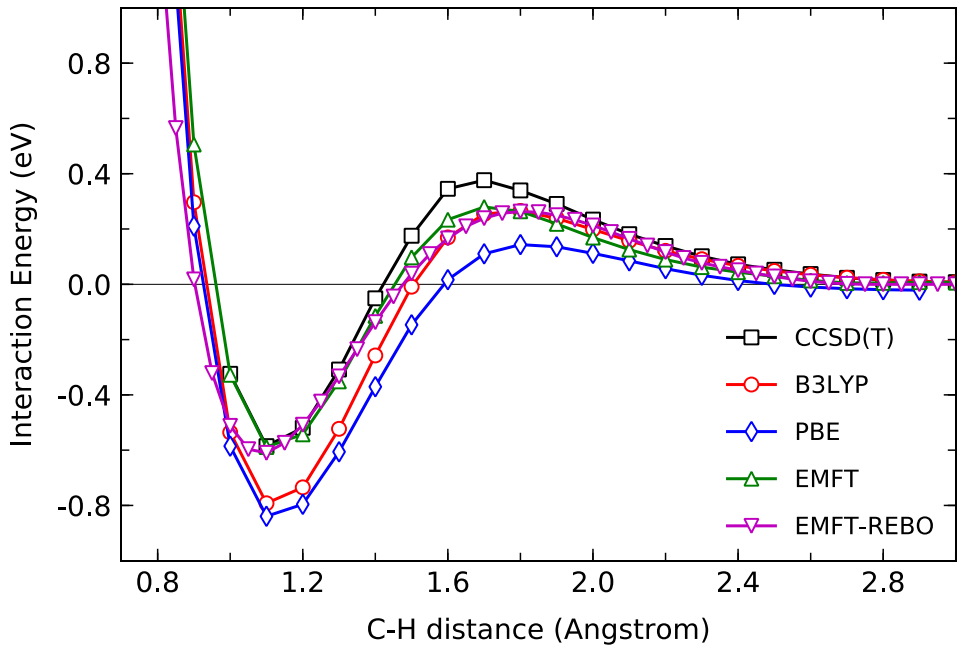

Figure S2. Calculated minimum energy path (MEP) for H atom on-top adsorption on free-standing graphene at various levels of theory. The levels of theory reported here are the same as in Table S1.

For the results in Table S1 and Fig. S2, the following system sizes were employed. The CCSD(T) results (*24*) were obtained for an H atom interacting with the coronene graphene flake, $C_{24}H_{12}$. The EMFT results and DFT results in the GTO basis were obtained for an H atom

interacting with a larger graphene flake, $C_{42}H_{16}$, and using 16 carbon atoms in the high-level subsystem for the EMFT calculations (Fig. S2); additional benchmarking results with larger graphene flakes are presented in *Section SI Computational Details 2*. The plane-wave DFT and EMFT calculations were performed with periodic boundary conditions, using a simulation cell with 24 carbon atoms arranged such that the surface consists of 3 by 4 primitive cells. A vacuum region of 13 Å above the graphene ensures that periodically stacked surfaces do not interact with one another.

For the results in Table S1 and Fig. S2, the chemisorption well depth and barrier height are examined in terms of the minimum energy path (MEP) along the on-top approach angle, which corresponds to the H atom approaching the center carbon atom from the direction normal to the graphene surface. The reported DFT B3LYP/cc-pVDZ, PBE/plane-wave, and EMFT-REBO energies are evaluated at geometries that were optimized at the same level of theory; specifically, all degrees of freedom are relaxed at each fixed value for the C-H distance. The reported CCSD(T)/cc-pVDZ and EMFT energies are evaluated at the B3LYP/cc-pVDZ-optimized geometries. The chemisorption well depth is computed as the electronic energy difference between the minimum along this MEP and the system at infinite H-graphene separation distance; the chemisorption barrier height is computed as the electronic energy difference between the maximum along this MEP and the system at infinite H-graphene separation distance.

In agreement with previous work (*24*), it is seen in Table S1 and Fig. S2 that the PBE/plane-wave result underestimates the barrier height for the H-graphene interaction relative to CCSD(T) by over a factor of two, whereas the B3LYP/cc-pVDZ description returns the calculated barrier height to with 0.1 eV of the CCSD(T) result. The EMFT description of the barrier height is essentially unchanged from that of the more costly B3LYP/cc-pVDZ calculations; the well-depth for the EMFT description at these geometries is slightly lower than that of B3LYP/cc-pVDZ, although it remains close to the CCSD(T)/cc-pVDZ description. Finally, the EMFT-REBO calculations, which are directly parameterized on the basis of the EMFT calculations, precisely reproduce both the EMFT barrier height and well depth. It is particularly notable that while the EMFT results are obtained at B3LYP/cc-pVDZ-optimized geometries while the EMFT-REBO results are obtained at EMFT-REBO-optimized geometries, the resulting MEPs are essentially identical at all C-H separations; this indicates that the shape of the EMFT-REBO, EMFT, and B3LYP/cc-pVDZ potential energy surfaces are all very similar, as is the goal of the methods. Taken together, these results indicate that the CCSD(T) results are

reproduced well using EMFT for this system, and they demonstrate the fidelity with which the EMFT-REBO results reproduce EMFT.

Computational details. 2. EMFT calculation details and benchmarking.

All EMFT calculations in the current study employ B3LYP-in-LDA embedding, with a high-level subsystem described using DFT with the B3LYP hybrid functional (*41-44*) and the cc-pVDZ basis set (*45*), while the surrounding environment is described using DFT with the LDA functional (*43*, *48*) and the minimal STO-3G basis set (*49*). The density-fitting approximation with the cc-pVDZ/JKFIT (*56*) basis is employed for evaluation of the electron repulsion integrals (*57*). Both the atomic-orbital and density-fitting basis functions are implemented as GTOs. All EMFT calculations are open-shell and employ spin-unrestricted orbitals. Benchmark studies confirm that a graphene flake of $C_{42}H_{16}$ is sufficiently large to describe the H-on-graphene interactions (Fig. S3) and confirm that a high-level subsystem comprised of the colliding H atom and the 16 carbon atoms is necessary (Fig. S4). Based on these benchmark results, all EMFT results were performed for a system with a graphene flake of $C_{42}H_{16}$ using 16 carbon atoms in the high-level subsystem (Fig. S5), as well as including the scattering H in the high-level region. Using these parameters, the computational cost of the B3LYP-in-LDA embedding description using EMFT is vastly reduced (over 11-fold) in comparison to the computational cost of the full calculation performed at the B3LYP/cc-pVDZ level (Table S2).

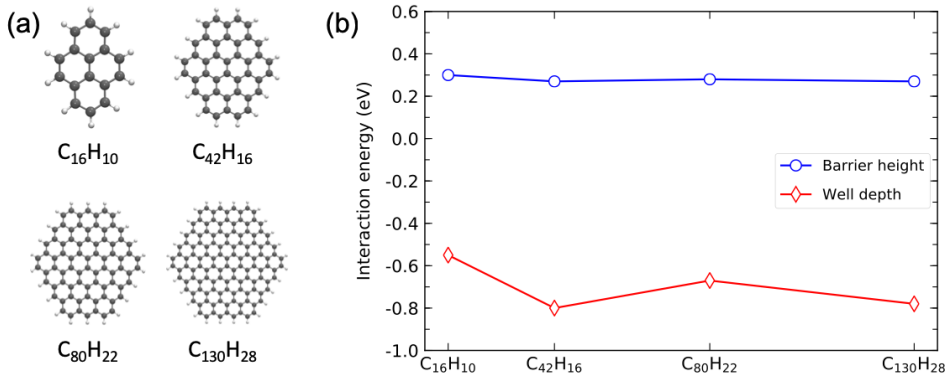

Figure S3. Graphene flake size dependence of chemisorption barrier height and well depth calculated at DFT B3LYP/cc-pVDZ level of theory. (a) graphene flakes studied in this work; (b) calculated chemisorption barrier height and well depth for different sizes of graphene flakes. All geometries are optimized at the DFT B3LYP/cc-pVDZ level of theory.

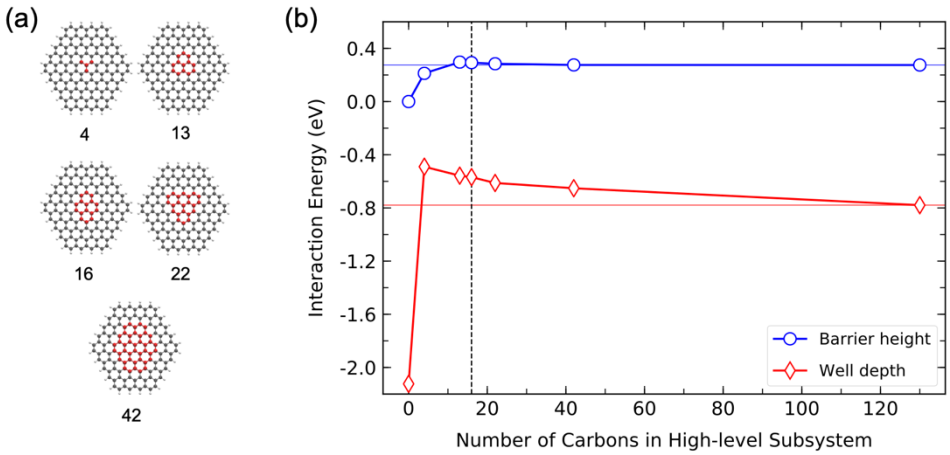

Figure S4. Accuracy of EMFT in chemisorption barrier height and well depth for the $C_{130}H_{28}$ graphene flake, relative to DFT B3LYP/cc-pVDZ level of theory. (a) Illustration of the different choices for the high-level subsystem that are considered; (b) EMFT barrier heights and well depths for different choices of the high-level subsystem. The blue horizontal line and red horizontal line correspond to DFT barrier height and well depth obtained at B3LYP/cc-pVDZ level of theory, respectively. The vertical dashed line corresponds to the high-level subsystem consisting of 16 carbon atoms. The relevant geometries are optimized at the B3LYP/cc-pVDZ level of theory.

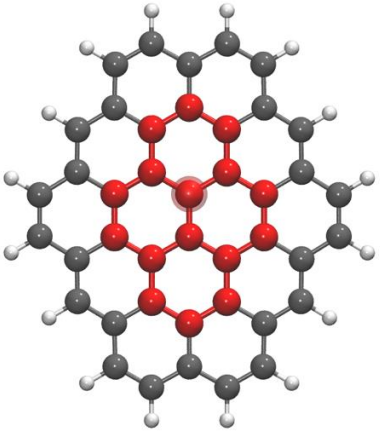

Figure S5. Partitioning of the $C_{42}H_{16}$ graphene flake for EMFT calculations. The atoms in red correspond to the high-level subsystem, and the remaining atoms correspond to the low-level subsystem. The carbon atom to which the H atom binds is highlighted.

Table S2. Timing comparison on single-point energy calculations using DFT and EMFT for H on $C_{42}H_{16}$ graphene flake.[a, b]

Method	Total time (seconds)	Relative speed-up
DFT[c]	521	1
EMFT	46	11.3

[a] Both calculations are performed using the same geometry optimized at the B3LYP/cc-pVDZ level of theory. For both calculations, convergence is achieved within 21 SCF iterations.
[b] Calculations are run on a NERSC Haswell computer with 32 cores and 128 GB DDR4 2133 MHz memory. Wall-clock times are reported.
[c] DFT calculation on full $C_{42}H_{16}$ flake at B3LYP/cc-pVDZ level of theory.

Computational Details. 3. Fitting REBO using EMFT molecular dynamics simulations.

Ab initio molecular dynamics (AIMD) simulations for the scattering experiment using EMFT provide reference energies and forces for training of the REBO potential. The $C_{42}H_{16}$ flake is used as the model system for graphene. We employ the EMFT subsystem partitioning with the high-level subsystem comprised of the colliding H atom and the 16 carbon atoms (Fig. S5). Initial conditions for AIMD trajectory calculations are set to mimic the experimental conditions and to sample the configuration space needed for parameterization of the REBO potential. These conditions include: (1) the initial coordinates and velocities of the graphene atoms, which are sampled from a pre-equilibrated trajectory of the graphene at 300K using Andersen thermostat; (2) the initial kinetic energy of the incident H atom is set to 1.92 eV; (3) the target positions of the incident H atom are randomly distributed within the central unit cell of the graphene flake; (4) the incident polar angles of the H atom range from 0° to 60° with 10° spacing; (5) the incident azimuthal angles range from 0° to 180° with uniform random distribution and (6) the initial H atom position is set 5 Å above the graphene surface.

In addition to the above trajectories, we also carry out simulations that start from the same initial conditions except that the initial H atom is put 1.2 Å above the graphene surface, in order to provide sufficient sampling for configurations that are near the chemisorption well and barrier. A total number of ~ 400 EMFT trajectories were performed and 1600 data points were used for the REBO parameterization.

The fit itself was performed with all three parts of the REBO PES, i.e., the C-C interaction, the projectile-graphene interaction, and the interaction between the graphene flake and its terminal H-atoms, being simultaneously fit. The parameters for the projectile H-atom and the graphene terminal H-atoms were treated separately, to avoid having the large number of terminal H-atoms unduly dominate the fitting; furthermore, the interaction between the graphene flake and its terminal H-atoms can be disregarded when performing MD simulations with periodic boundary conditions which eliminate the graphene terminal H-atoms. The fits were done with the trust-region nonlinear least squares algorithm and convergence was achieved typically after 12 local optimization steps. For each fit, the initial parameters were selected by applying a Gaussian blur of 15% to each REBO parameter from the original publication, resulting in an optimization in 27 dimensions.

The success of the re-parametrization is judged by several criteria. First, the root mean square error (RMSE) must not differ much between the training and validation data; if the RMSE to the training data was much lower than to the validation data, this would indicate overfitting.

The selected PES has an RMSE to the training data of 169 meV and the validation data can be reproduced with an RMSE of 183 meV. Second, the carbon cohesive energy should not deviate excessively from literature values; the employed PES predicts a cohesive energy of 12.3 eV for a carbon atom, while literature values range from 7-9 eV (*58*, *59*). Third, cuts through certain dimensions of the PES can be compared to reference calculations (see Fig. S3); the re-parametrized REBO PES should be able to accurately predict energetic changes during the adsorption process, i.e., barrier height, chemisorption well depth, and the correct positions of both with respect to C-H distance from a top-site on the graphene surface.

Computational Details 4: Ring-polymer molecular dynamics

Ring-Polymer Molecular Dynamics (RPMD) is an approximate quantum dynamical method that is based on Feynman's imaginary-time path integral formulation of statistical mechanics (*26*, *60*). RPMD enables quantum simulation via direct dynamics by providing a classical molecular dynamics model for the real-time evolution of a quantum mechanical system. The RPMD trajectories both preserve the exact quantum Boltzmann distribution and exhibit time-reversal symmetry. The method has been demonstrated for the description of dynamics associated with both thermal equilibrium initial conditions (*26*), as well as special cases of non-equilibrium initial conditions (*27*). In the current study, we employ the "momentum impulse" non-equilibrium conditions to describe graphene sheet at thermal equilibrium at 300 K but with the colliding H atom initialized with a specified incident kinetic energy (*27*); in this protocol, the internal modes for the H-atom ring polymer are initially equilibrated at a temperature of 300 K, while the centroid mode of the H-atom ring polymer is initialized with the velocity corresponding to the incident kinetic energy. The simulations were found to be sufficiently converged using 12 ring-polymer beads. The thermalized initial distribution for the graphene sheet was obtained using the path integral Langevin thermostat (*61*). In terms of the position of the H atom, the RPMD scattering trajectories were initialized in the same way as for the classical MD simulations, except with the position of the classical H atom replaced by the centroid position of the ring polymer, and the scattering angle and final kinetic energy for the RPMD trajectories were likewise determined from the centroid of the H-atom.

S2. The influence of the Pt substrate on the H atom scattering

Graphene primarily interacts with a Pt(111) surface through weak dispersion forces (*23*). The EMFT-REBO approach just described was modified to include the effect of the Pt substrate on the experimental observables. The substrate was modelled in the simulations using Lennard-Jones (LJ) potential interactions with each atom in the graphene layer. Specifically, carbon

atoms in the graphene layer experience pair-wise interactions with a single layer of Pt atoms that simulates the surface, via a potential of the form $V(r)=4\varepsilon*[(\sigma/r)^{12}-(\sigma/r)^{6}]$, where r is the Pt-C distance, ε = 250 K and σ = 2.95 Å. This choice of parameters yields an interaction energy between the Pt and graphene layers of 70 meV per C atom, which is consistent with literature values (*62*).

Figure S6 shows the influence of this model of Pt-graphene interactions on the sticking probabilities. For both incidence energies studied in this work, the sticking probability is slightly enhanced at low E_I and slightly reduced at high E_I. For a finite surface temperature puckering is enhanced compared to free-standing graphene by the asymmetry of the LJ potential. This permits H atoms to more easily overcome the adsorption barrier. Indeed, when all degrees of freedom are allowed to relax, the minimum energy path to adsorption takes place over a barrier that is 60 meV lower than on free-standing graphene. Meanwhile, the pre-puckering also results in a slightly smaller energy loss resulting in slightly less sticking at high E_n.

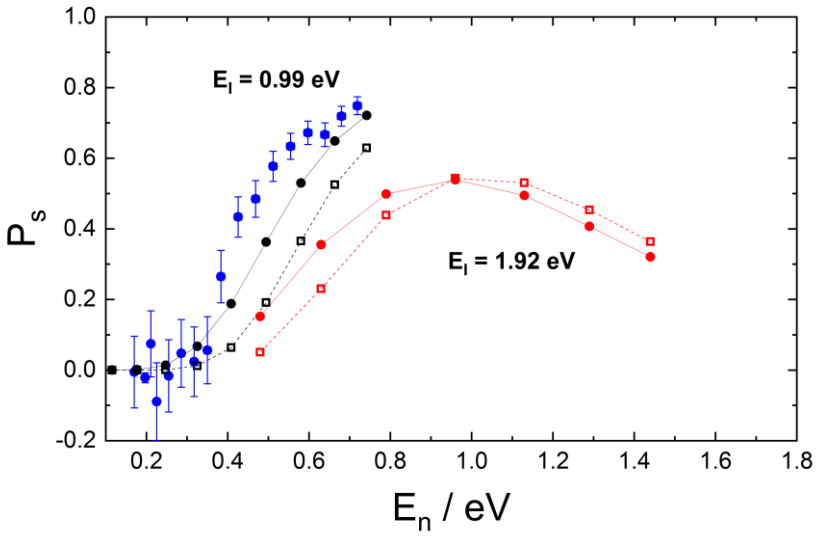

Figure S6: Influence of Pt substrate on sticking probability. Experimentally derived (blue) and theoretically predicted (black) sticking probabilities for $E_I = 0.99$ eV at various incidence angles in units of normal incidence energy (E_n). Results are for two cases: neglect of Pt (dashed lines, open symbols) versus inclusion of Pt by Lennard-Jones potential of van der Waals forces (solid lines, solid symbols). For $E_I = 1.92$ eV, the corresponding theoretical sticking probabilities are also presented (red), both neglecting (dashed lines, open symbols) and including (solid lines, solid symbols) the Pt substrate.

S3. Out-of-detection-plane scattering

The experimental data is only sensitive to H atom scattering that occurs in a detection plane containing a vector along the initial H atom beam direction and a vector pointing from the H atom impact point on the graphene sample to the detector. The normal vector of this detection plane is parallel to the rotation axis of the detector. Figure S7 shows representations of

scattering simulations demonstrating the importance of scattering outside of the instrumental detection plane. Here, the instrument detection plane corresponds to all values of ϑ where φ = 30°.

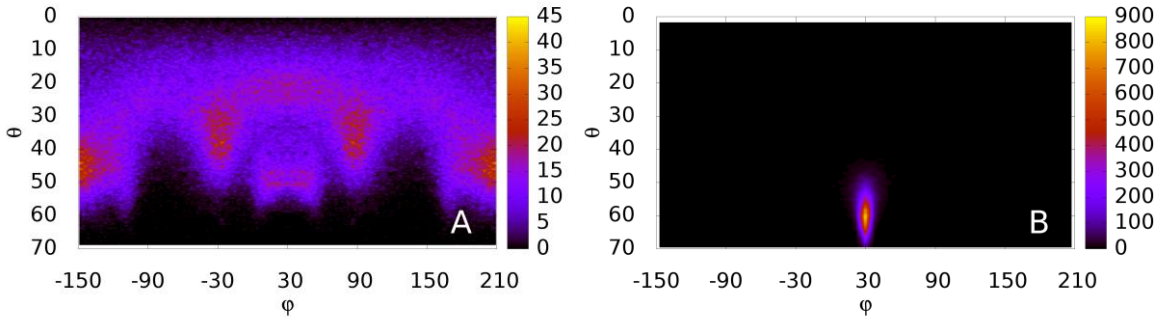

Figure S7: Azimuthal scattering fluxes calculated from MD on the EMFT-REBO PES assuming a single rotational orientation of the graphene crystal. Here the initial conditions are: E_I =1.92 eV, T_S =300K. **(A) transient chemical bond formation channel** exhibiting scattering outside of the detection plane, ϑ_I =30°, φ_I =30°, and **(B) quasi-elastic channel** exhibiting scattering primarily within the detection plane ϑ_I =60°, φ_I =30°. φ_I =0° corresponds to H atom trajectories whose velocity vector projection onto the graphene plane aligns with a C=C. φ_I = 30° corresponds to H atom trajectories whose velocity vector projection onto the graphene plane aligns perpendicular with a C=C.

For the slow channel where a transient chemical bond is formed, the MD calculations on the EMFT-REBO PES show significant scattering probabilities out of the detection plane, when the incidence angle ϑ_I =30° & φ_I = 30° (see Fig. S7-A). At this value of φ_I, the projection of the H atom velocity vector onto the graphene plane is orthogonal to C=C bonds. The calculations predict a large amount of H atom flux out of the detection plane by this oriented collision. By contrast, the quasi-elastic channel shown in Figure S7-B, does not show this effect; here, ϑ_I =60° & φ_I = 30° mainly gives rise to scattering within the detection plane. A similar behavior can also be seen in theoretical predictions of the φ_I-dependence of the in-plane scattering probability, Fig. S8. In-plane scattering is largest when the projection to the incident H atom trajectory on the graphene plane aligns with a C=C and it is smallest, when the trajectory is aligned orthogonal to C=C bonds.

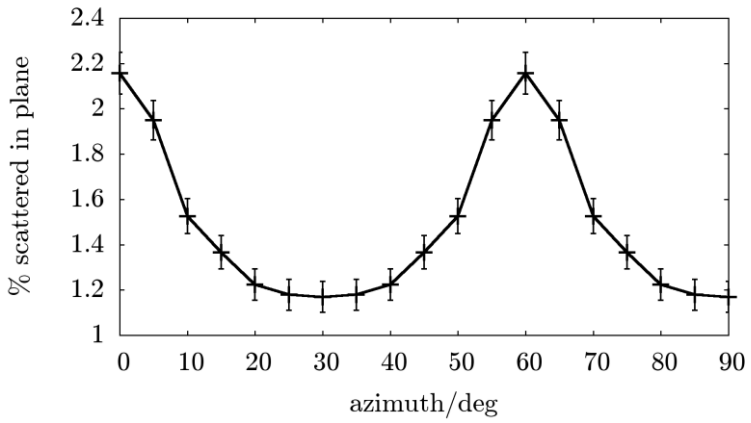

Figure S8: Azimuthal dependence of the in-plane signal. Crosses are calculated values and error bars indicate the 95% confidence interval. 0° and 60° are parallel to C=C bonds, and 30° and 90° are orthogonal to them. Incidence conditions are E_I=1.92 eV, ϑ_I =45°, where changes in the in-plane signal can be attributed to out-of-plane deflection during transient bond formation.

The graphene samples used in the experiments are not single crystals; they are composed of two equally abundant orientational domains, one rotated by 27° with respect to the other. Each domain has an orientational distribution of Gaussian with a width of ~5˚. The experimental data was acquired with φ_I =13.5°, where the H atom velocity vector is oriented symmetrically with respect to these two orientational domains. To simulate experimental results, both on sticking probabilities for E_I=1.92 eV presented in Fig. 3 and measured scattering fluxes shown in Fig. 2, we have carried out calculations averaging over two rotational domains oriented with φ_I =13.5°. Figure S9 shows how the out of plane structure in the scattering angular distributions is averaged out in scattering through the two domains.

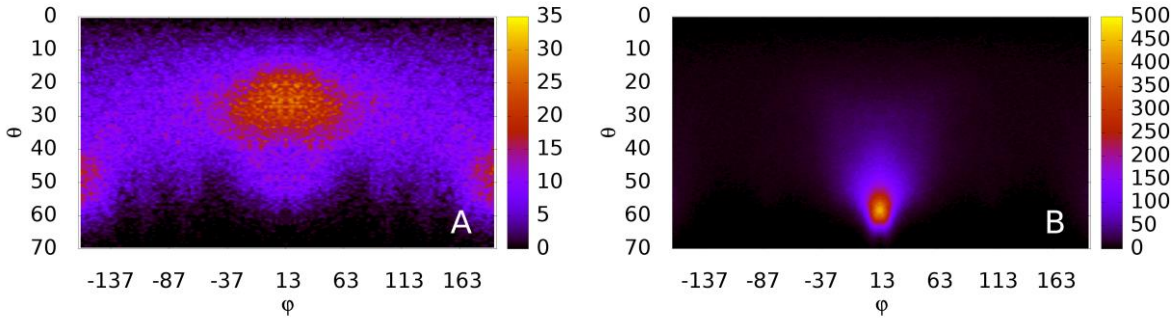

Figure S9: Scattering fluxes calculated from MD on the EMFT-REBO PES averaging over two orientational domains of the graphene crystal. (A) transient chemical bond formation channel present at ϑ_I =30° exhibiting scattering outside of the detection plane and **(B) quasi-elastic channel** seen at ϑ_I =50° exhibiting scattering primarily within the detection plane. Here the initial conditions are: E_I =1.92 eV, φ_I 13.5°, T_S =300K. The mechanical influence of the Pt-substrate was also taken into account (see Sec. S2).

S4. H atom sticking probabilities at $E_I = 0.99$ eV

It is best to attempt an experimental determination of sticking probabilities where the scattering in the slow channel is unimportant, otherwise a careful and accurate accounting of out of detection plane scattering must be a part of the analysis. By lowering the incidence energy to E_i = 0.99 eV, where no slow channel is observed, we are able to observe the survival probability of the quasi-elastic channel as a function of normal incidence energy. Figure S10 shows a comparison of experiment and theory for E_i = 0.99 eV at three incidence angles. No slow channel is seen because the energy dissipation for low energy H atoms that cross the barrier to C-H bond formation is so efficient that re-crossing and escape back to the gas-phase does not occur. We can then use the experimental data to obtain the integrated scattered flux in the fast channel as a function of incidence angle, which is shown in Fig. S11. The survival probability increases as the normal component of incidence energy drops, reaching a plateau below $E_n = 0.35$ eV. Here we set the survival probability to 1 and use this to extract the sticking probability shown in Fig. 3 of the main text.

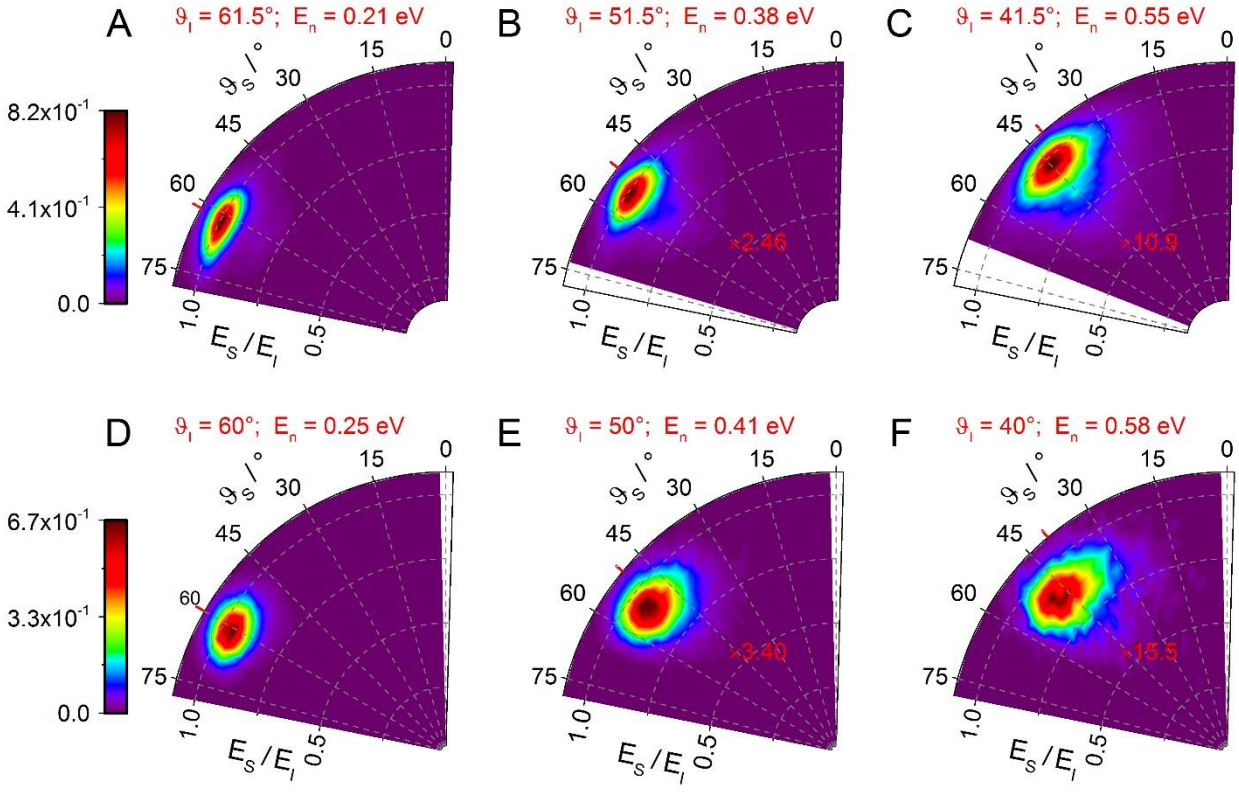

Figure S10: Scattering distributions of H collisions with graphene at $E_I = 0.99$ eV. **A-C** show measured H atom scattering energy, E_S, and angular, ϑ_S, distributions. Each distribution is multiplied by the indicated red number to use the same color bar. **D-F** show corresponding simulated scattering distributions. The incidence angles, ϑ_I and normal incidence energy, E_n, are also indicated ϑ_S =0 indicates the surface normal direction. Red ticks indicate the specular scattering angles. All observed scattering occurs within the plane defined by incident H atom beam and the surface normal.

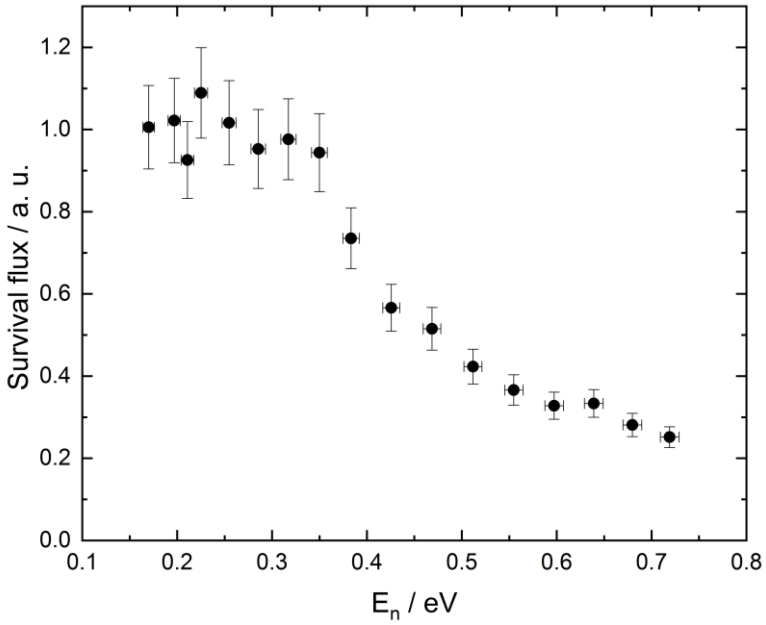

Figure S11: Experimentally derived survival flux using the data like that shown in Fig. S10.

This procedure requires an accounting of how the scattering angular distribution changes with incidence angle. The angular distributions in the plane of detection are shown in Fig. S12A-C (experiment) and S12D-F (theory).

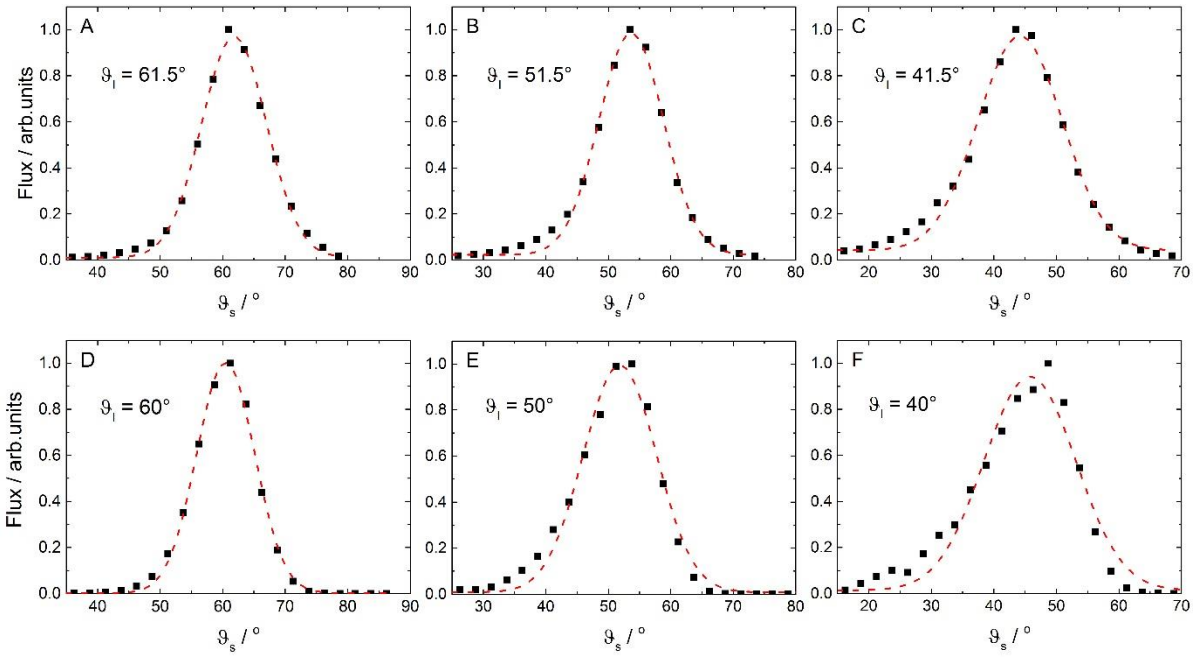

Figure S12: Experimental (A-C) and Theoretical (D-F) angular distribution of H atom scattering from graphene integrated over energy loss. The incidence conditions are the same with Fig. S10. Red dashed lines are Gaussian fits.

We integrate over the out-of-detection plane angles assuming cylindrical symmetry of the angular distributions; Fig. S13 shows theoretical predictions that justify this assumption.

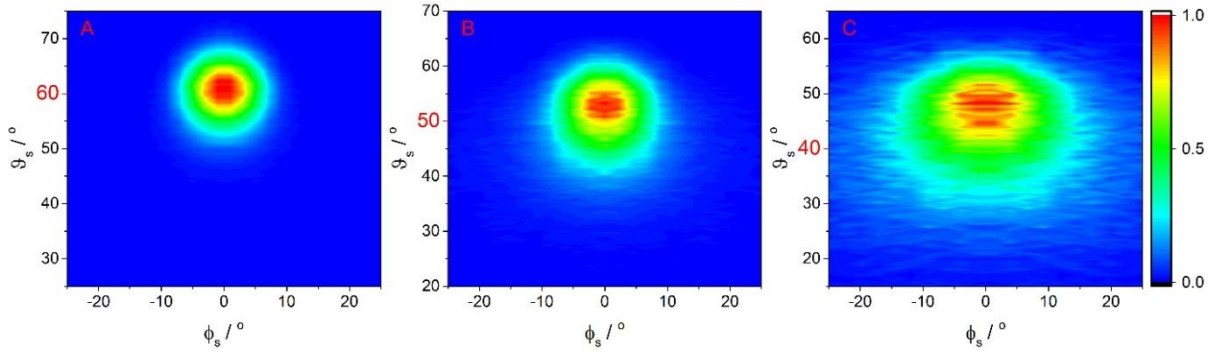

Figure S13: Calculated in-plane and out-of-plane angular distribution of H atom scattering from graphene integrated over energy loss. The incidence conditions are the same with Fig. S10 **D**-**F**. ϕ_s is the angle of the scattering direction relative to the plane defined by the incidence beam and surface normal. Scattering at $\phi_s = 0^\circ$ corresponds to in-plane scattering.

S5. A critical comparison of experiment and theory

In Figure 2 of the main text, we uniformly shifted the simulated scattering flux distributions by 10° in order to emphasize the similarities between the experiment and simulations. Figure S14 shows the same comparison as in Fig. 2 without the 10° shift; here, incidence angles differ by less than 1°. The simulation agrees well with experiment at angles where only one channel is present: ϑ_I = 60° shows only the fast channel and ϑ_I = 30° only slow channel. For the intermediate angle, both channels are present in simulations and experiment, but the simulations overestimate the fast component's relative contribution to the scattering signal.

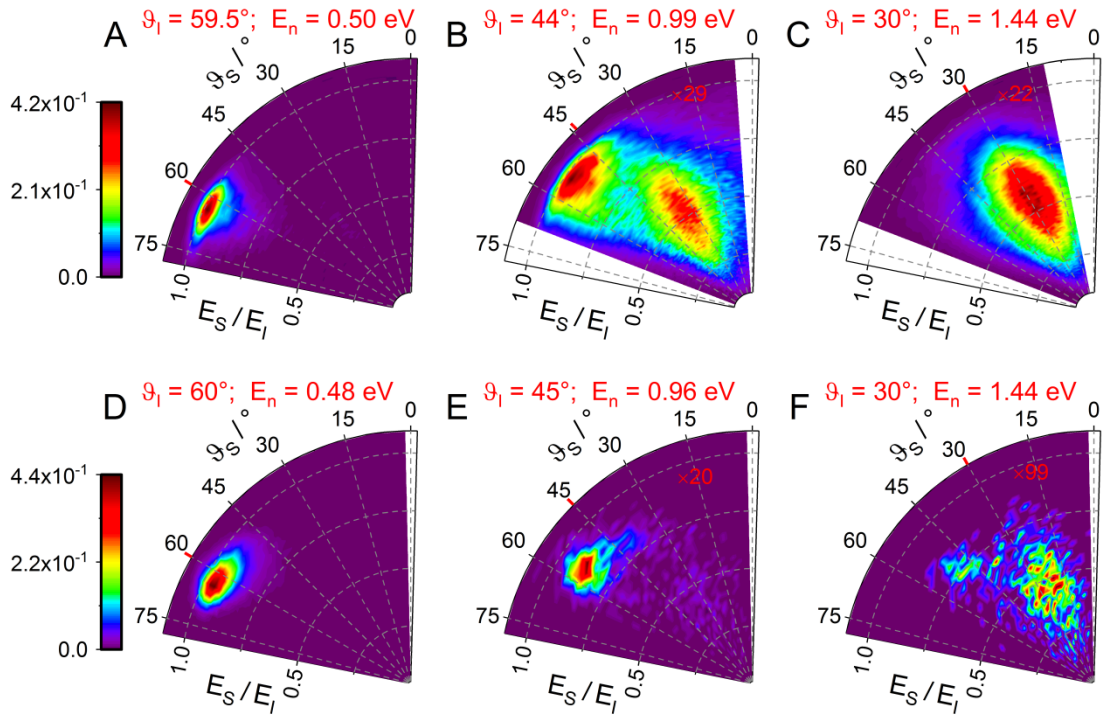

Figure S14: Scattering distributions of H collisions with graphene. **A-C** show measured H atom scattering energy, E_S, and angular, ϑ_S, distributions with $E_I = 1.92$ eV scattering. Each distribution is multiplied by the indicated red number to use the same color bar. **D-F** show corresponding simulated scattering distributions. The incidence angles ϑ_I and normal incidence energy, E_n, are indicated. ϑ_S =0 indicates the surface normal direction. Red ticks indicate the specular scattering angles. All observed scattering occurs within the plane defined by incident H atom beam and the surface normal.

These observations also appear in the angle-integrated energy loss distributions - Fig. S15. Again, there is excellent agreement between the simulations and experiment at ϑ_I = 60° and 30°, while the intermediate angle is biased towards the fast component.

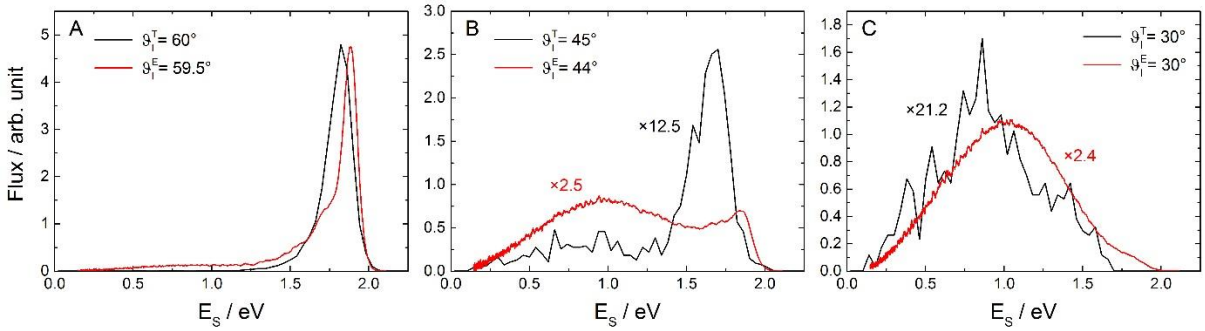

Figure S15: Energy distribution for H atom scattering within the detection plane integrated over all polar scattering angles. The incidence conditions are the same with Fig. S14. ϑ_I^T and ϑ_I^E are incidence angles for theoretical simulation and experimental measurement, respectively. The multiplying factor indicates the signal drop.

The results in both Figs. S14 and S15 suggest that, despite broad agreement between the simulations and experiment, the simulations predict a slightly higher energy threshold for C-H bond

formation than is seen in experiment. Evidence of this bias also appears in the predicted sticking probabilities shown in Fig. 3, with the simulations requiring slightly more incidence energy to overcome the barrier to C-H bond formation. These discrepancies could arise from inaccuracies in the potential energy surface - possibly from the employed electronic structure methods or the simplicity of the description of the Pt-graphene interactions. For example, the increased degree of covalent bonding between graphene and Pt(111) that becomes possible when a C-H bond is formed is not included in our treatment and will likely deepen the C-H binding well and slightly lower the barrier as well.

Another possible source of discrepancy between experiment and simulation is the effect of out-of-detection-plane scattering - see section S3. To the extent that the simulations do not reproduce the scattering flux in both the fast and slow channels, the apparent branching between the two would differ from experiment. While the scattering effects reported here emerge only from our theoretical analysis, the possible errors associated with azimuth-specific scattering are likely to be small. We note that recent measurements on single crystal graphene grown on Nickel show clearly that there is an influence of azimuthal incidence angle on scattering probability (*63*). Moreover, the samples in the present work were polycrystalline; hence, they represent an average over two crystal orientations, an experimental condition that tends to wash out the influence of azimuthal specificity.

With these considerations in mind, we have allowed ourselves a global 10° shift in the polar angle of Fig 2 to emphasize the broad similarities between the simulated and experimental results. More important than the above described discrepancies, in our view, is that the energy loss predicted by the theory is nearly identical to that of experiment, as is clear from Figs. S15 A&C. It is for this reason that excellent agreement between simulation and experiment is obtained for the sticking probabilities in Fig. 3, where we duly note that no global polar angle shift has been introduced.

S6. Sonic wave energy transport

Fig. S16 shows the time dependent displacement of carbon atoms involved most directly with the H atom during the collision. As in Fig. 4, carbon atom shells are used to group neighboring atoms. When the H atom induced sp^2-sp^3 re-hybridization of the 0^{th} shell C-atom occurs, the length of its bonds to neighboring C atoms changes. As a consequence, the carbon atoms in the 1^{st} shell are initially pushed away from the center of impact. In turn, the second shell carbon atoms are also deflected. This process continues and a wave propagates through the graphene sheet. By monitoring the C-atom's displacements during simulation, we calculate the speed of

this wave to be ~18.6 km/s. This is similar to graphene's in-plane speed of sound (22 km/s) determined by analysis of the LA phonon branch (*29*). This agreement with our simulations also argues for the overall accuracy of our EMFT-REBO PES.

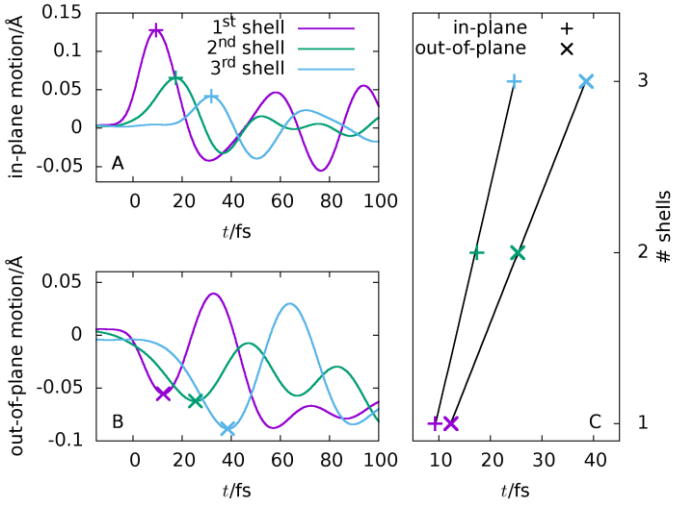

Figure S16: Sonic wave energy dissipation. A) In-plane deflection of C-atoms in different shells from their respective equilibrium distance to the C-atom struck by the projectile. The maximum amplitudes are marked by pluses. Time zero is defined as the time of H atom closest approach. These results are the average of the 60 selected trajectories shown in Fig. 4B. **B)** Out-of-plane deflection of the carbon atoms in the same shells as in panel A. **C)** Points in time when the marked extrema in panel A and B are observed. From a least squares fit the speed of the outgoing waves is calculated to be 18.6 km/s in-plane and 10.9 km/s out-of-plane.

S7. The hard cube model, the quasi-elastic channel and the site specificity of sticking

Figure S17 shows a dynamical feature of the fast channel observed in this study that is markedly different from the dynamics of the slow channel. Here, we compare predictions of the hard cube model to experimental data for the fast channel. The hard cube model envisions the H atom of mass *m* colliding with a flat surface of mass *M* at an incidence angle ϑ_I. The model conserves momentum parallel to the surface allowing one to show that the energy loss ΔE, is given by the following formula.

$$\Delta E = E_I - E_S = \left[\frac{4Mm}{(M+m)^2}\right] E_I cos^2\vartheta_I = \left[\frac{4Mm}{(M+m)^2}\right] E_n$$

Here *M* is the only adjustable parameter to fit the data (the red and black solid lines in Fig. S17).

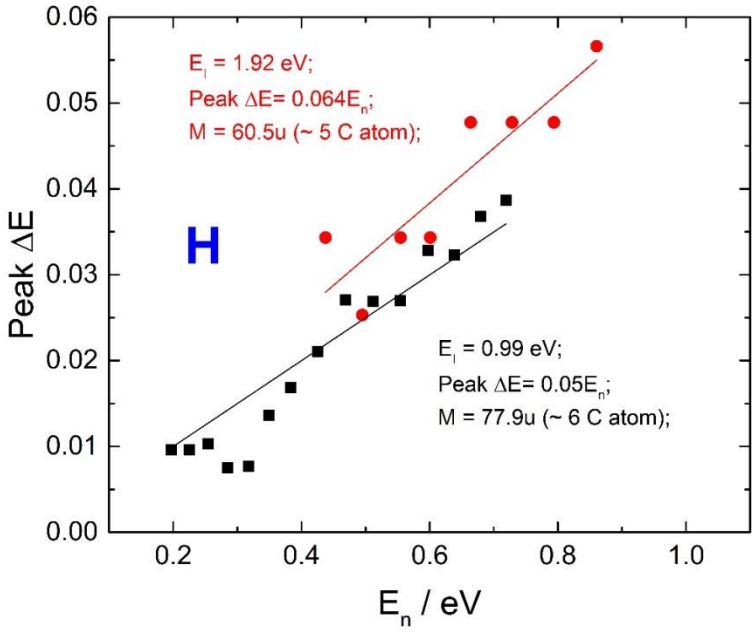

Figure S17: Most probable energy loss for the fast channel at various incidence angles in units of normal incidence energy E_n. Solid lines are fittings according to a hard cube model. Symbols are derived from experiment.

The effective mass of the hard cube, M, is close to the mass of 5-6 Carbon atoms. This suggests that for the quasi-elastic channel, the H atom interacts with a six membered ring of C-atoms.

The site-specific sticking probabilities, shown in Figure S18 for several incidence energies help to explain this. At E_n =0.5 eV, sticking is more likely for collisions directly over C-atoms, where the barrier is lowest. Conversely, quasi-elastic scattering occurs when H atoms collide away from C-atoms, that is, for collisions over the center of the six membered rings. As the incidence energy increases to E_n =1 eV, the sit-specific restrictions for sticking relax. Conversely, the site specificity of the quasi-elastic channel increases. Here, the quasi-elastic channel results from an impact precisely at the center of a six membered C-ring, where the H atom is simply too far from any C atom to interact specifically with a single atom. Instead, the picture emerges that the quasi-elastic channel resembles a collision with a rigid six membered C atom ring.

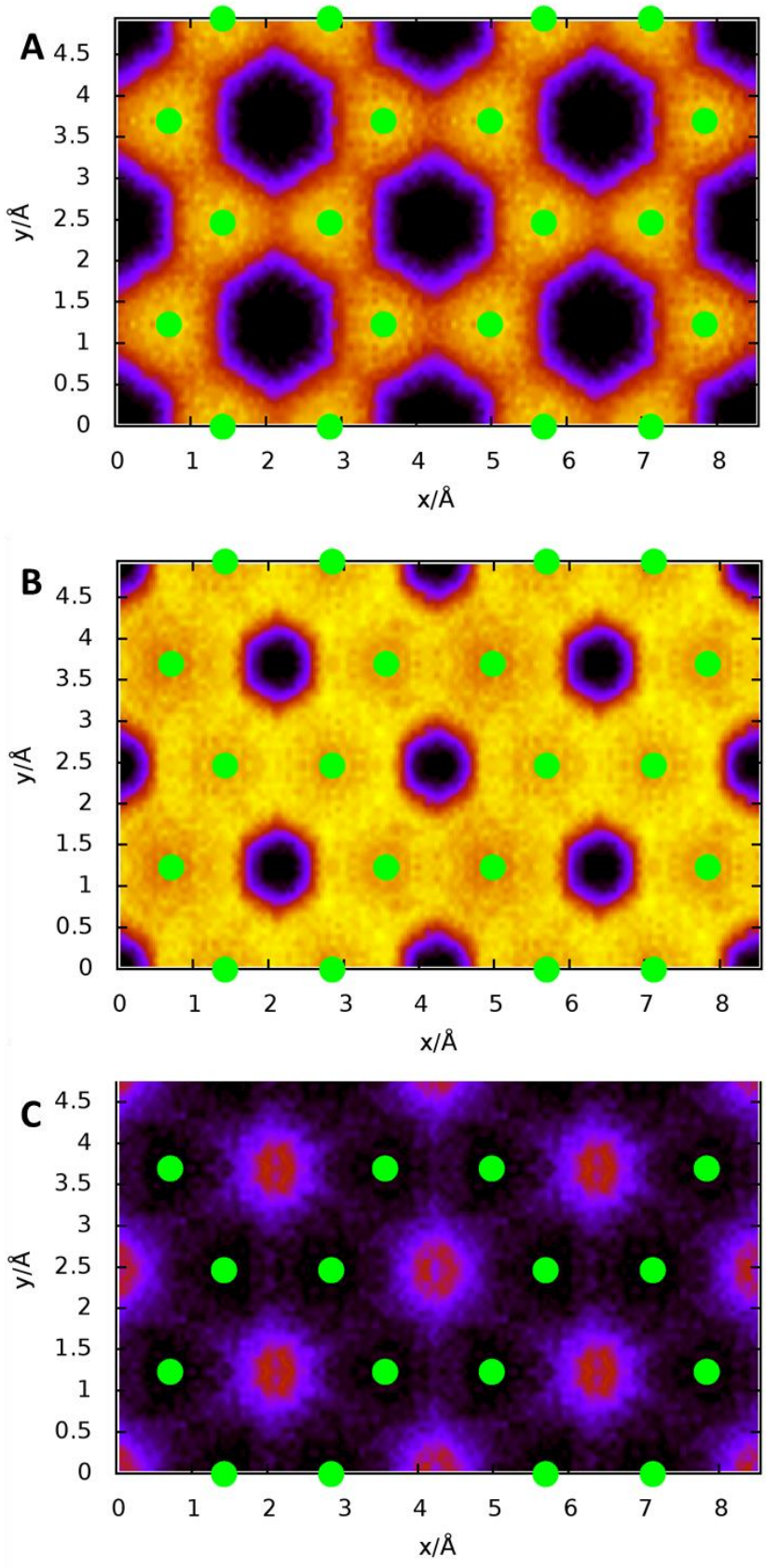

Figure S18: Heat Map representation of the site specific sticking of H atoms at graphene versus H atom incidence energy. A) $E_I = 0.5$ eV (near threshold). **B)** $E_I = 1.0$ eV (sticking probability maximum). **C)** E_I =2.0 eV (incidence energy too high for efficient sticking). Incidence direction is along the surface normal. Green filled circles indicate position of C atoms. Increasing brightness of the color denotes increasing sticking probability.

At high incidence energies sticking and slow channel scattering dominate and compete with one another. It is easy to understand that at $E_I = 0.5$ eV, only H-atoms that directly collide on top of C atoms can stick. Top sites have the smallest adsorption barrier height and H atoms that collide on other sites do not have enough energy to overcome the barrier. Furthermore, the H atoms that pass over the barrier have low energies that dissipate rapidly into the graphene. At high incidence energies, crossing the barrier is necessary but not sufficient for sticking; dissipating the excess energy is also necessary. As can be seen in Fig. S18, directly hitting the C atom no longer leads to the maximum probability for H atom sticking. In fact, at $E_I = 2.0$ eV, sticking is only possible when the H atom avoids the top site. This allows some of the normal incidence energy to be channeled into kinetic energy parallel to the surface, an effect that suppresses re-crossing of the barrier.

S8. Comparison to previous sticking probability work

Figure S19 compares the sticking probabilities emerging from our experimentally validated first principles calculations to those previously reported. The four previous reports all show lower sticking probability than is found in this work. This deviation is larger at higher incidence energies.

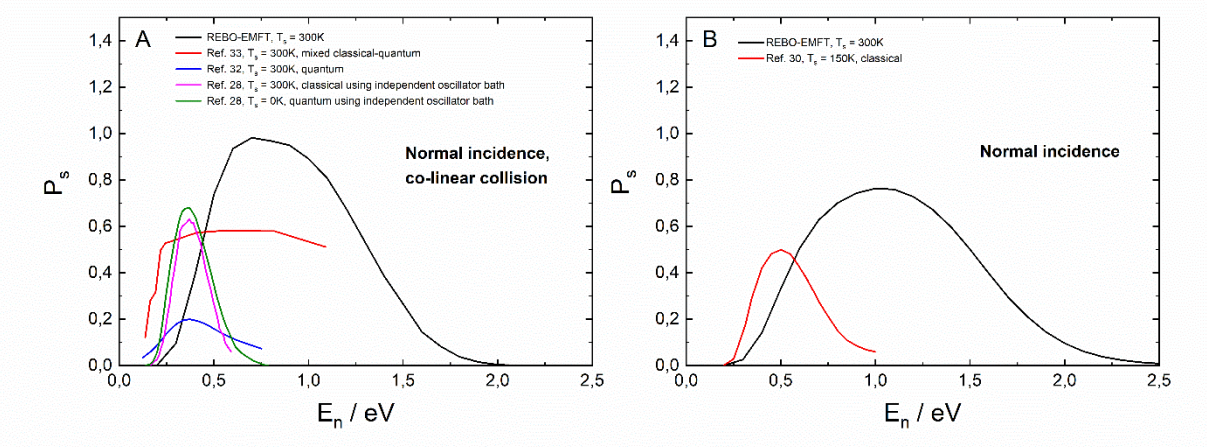

Figure S19: Comparison of theoretically predicted H sticking probabilities on graphene. A shows the H atom sticking probability for normal incidence and co-linear collision. T_s indicates the surface temperature in the simulation. E_n indicates the normal incidence energy (also the incidence energy). **B** shows the H atom sticking probability for normal incidence, and averaged over all impact parameters.

All of the methods (except that of Lemoine) appear to overestimate the sticking probability at low energy and all methods underestimate the sticking probability at high energy. While the previous studies all used different approaches, in light of the present work they all suffer from a common flaw: they only consider the Z direction movement of the C atoms. Some also only

consider the Z motion of the H atom as well. In short, all of these approaches used reduced dimensionality approximations that explicitly ignore concerted in-plane C-atom motion that leads to the high H atom translational inelasticity seen in this work. In fact, even the most recent reduced dimensionality theory agrees well with an impulsive collision model (*28*). This differs starkly from the dynamics seen in our work. Furthermore, the use of DFT at the GGA level to obtain input about the potential energy surface clearly results in a barrier to C-H bond formation that is too low - this is likely the explanation for the overestimated sticking probability at low energy seen in several of the studies.

S9. Classical simulations of IVR lifetimes

Conventional IVR experiments utilize optical excitation of a molecule initially at its equilibrium configuration. For the H graphene system, we seek to simulate such an experiment by initiating classical trajectories from an initial geometry that differs from the minimum energy structure only by the displacement of the H atom. This initial state resembles one produced by pumping a high overtone of the C-H stretch. To describe this, we set up the following simulation.

H adsorbed on a graphene surface is equilibrated in phase space to 300 K using the Andersen thermostat (*64*) in an NVT ensemble. Next, an NVE ensemble is simulated for 100 ps from which a snapshot is taken every 100 fs. Then, in each of the 1000 snapshots, the H atom is relaxed to the chemisorption well via the FIRE algorithm (*65*) while keeping all other degrees of freedom fixed. This completes the stage of preparation of an ensemble of initial conditions for the C atoms. Then for each initial total energy, we run 4500 NVE trajectories for 10 ps. A trajectory is initialized by first selecting one of the geometry-optimized snapshots and displacing the H-atom a certain distance either towards or away from the closest C-atom. This distance is randomly drawn from a uniform distribution ranging from -0.2 to 0.2 A. Next, the change in potential energy is calculated and if it is lower than the total energy of the simulation, the geometry is accepted and the remaining energy is provided as kinetic energy to the H-atom, letting its initial velocity vector randomly either point towards the graphene sheet or away from it. Finally, the trajectory is started in the NVE ensemble and the kinetic energy of the H-atom is saved every 0.1 fs. To obtain the time-scales of IVR for the set of initial kinetic energies, we average the kinetic energy of the H-atom in each time step over all trajectories in which it remained attached to graphene. Dissociation was observed in less than 150 trajectories at any initial energy and the results are shown in Fig. S20A.

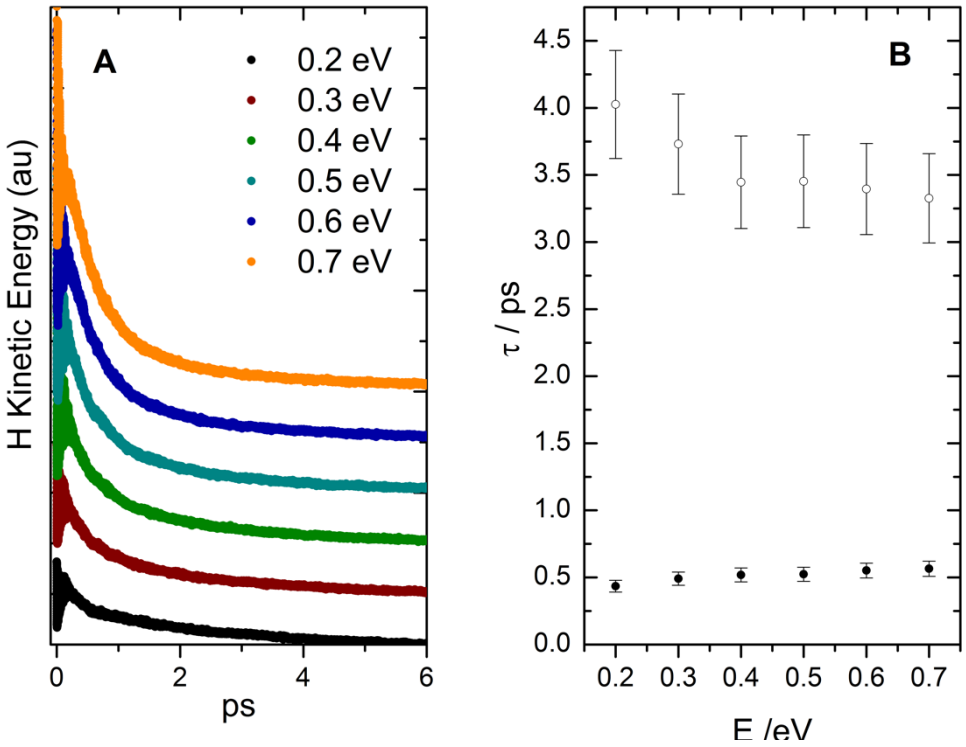

Figure S20: Classical Simulations of Intramolecular Vibrational Relaxation. A shows the H atom kinetic energy versus time at various initial energies. The plots are offset vertically from one another for clarity. Initially all energy is in either potential of kinetic energy of the H atom. The flow of H atom energy to the graphene slab takes place on the ps time-scale. The time dependence is best fit by a bi-exponential decay; the exponential lifetimes of the two process are shown in **B**. The error bars are estimated to be 10% of the lifetimes' values and they are mainly due to oscillations in the averaged data at early times.

The IVR follows a bi-exponential decay. It is comprised of a fast process that takes place in approximately 0.5 ps and seems to decelerate toward higher energies and slow process taking place on the order of several picoseconds- see Fig. S20B.

Movie S1: Animation of H impinging on graphene. The deep binding well develops only after the H atom has reached its point of closest approach.

References and Notes

1. B. S. Rabinovitch, J. D. Rynbrandt, Intramolecular energy relaxation—Nonrandom decomposition of hexafluorobicyclopropyl. *J. Phys. Chem.* **75**, 2164–2171 (1971). doi:10.1021/j100683a017

2. P. M. Felker, A. H. Zewail, Direct picosecond time resolution of dissipative intramolecular vibrational-energy redistribution (IVR) in isolated molecules. *Chem. Phys. Lett.* **108**, 303–310 (1984). doi:10.1016/0009-2614(84)85196-9

3. J. C. Keske, B. H. Pate, Decoding the dynamical information embedded in highly mixed quantum states. *Annu. Rev. Phys. Chem.* **51**, 323–353 (2000). doi:10.1146/annurev.physchem.51.1.323 Medline

4. J. D. McDonald, Creation and disposal of vibrational energy in polyatomic-molecules. *Annu. Rev. Phys. Chem.* **30**, 29–50 (1979). doi:10.1146/annurev.pc.30.100179.000333

5. M. Gruebele, R. Bigwood, Molecular vibrational energy flow: Beyond the Golden Rule. *Int. Rev. Phys. Chem.* **17**, 91–145 (1998). doi:10.1080/014423598230117

6. D. J. Nesbitt, R. W. Field, Vibrational energy flow in highly excited molecules: Role of intramolecular vibrational redistribution. *J. Phys. Chem.* **100**, 12735–12756 (1996). doi:10.1021/jp960698w

7. A. A. Stuchebrukhov, R. A. Marcus, Theoretical-study of intramolecular vibrational-relaxation of acetylenic CH vibration for $v = 1$ and 2 in large polyatomic-molecules $(CX_3)_3YCCH$, where x = H or D and Y = C or SI. *J. Chem. Phys.* **98**, 6044–6061 (1993). doi:10.1063/1.464843

8. J. M. Parson, Y. T. Lee, Crossed molecular-beam study of $F+C_2H_4$, C_2D_4. *J. Chem. Phys.* **56**, 4658–4666 (1972). doi:10.1063/1.1677917

9. T. Yang, J. Chen, L. Huang, T. Wang, C. Xiao, Z. Sun, D. Dai, X. Yang, D. H. Zhang, Reaction dynamics. Extremely short-lived reaction resonances in Cl + HD ($v = 1$) → DCl + H due to chemical bond softening. *Science* **347**, 60–63 (2015). doi:10.1126/science.1260527 Medline

10. J. Srinivasan, T. C. Allison, D. W. Schwenke, D. G. Truhlar, Transition state resonances in the reaction $Cl+H_2$ → HCl+H. *J. Phys. Chem. A* **103**, 1487–1503 (1999). doi:10.1021/jp984549k

11. J. W. Lu, B. S. Day, L. R. Fiegland, E. D. Davis, W. A. Alexander, D. Troya, J. R. Morris, Interfacial energy exchange and reaction dynamics in collisions of gases on model organic surfaces. *Prog. Surf. Sci.* **87**, 221–252 (2012). doi:10.1016/j.progsurf.2012.07.002

12. O. Bünermann, H. Jiang, Y. Dorenkamp, A. Kandratsenka, S. M. Janke, D. J. Auerbach, A. M. Wodtke, Electron-hole pair excitation determines the mechanism of hydrogen atom adsorption. *Science* **350**, 1346–1349 (2015). doi:10.1126/science.aad4972 Medline

13. S. M. Janke, D. J. Auerbach, A. M. Wodtke, A. Kandratsenka, An accurate full-dimensional potential energy surface for H-Au(111): Importance of nonadiabatic electronic excitation

in energy transfer and adsorption. *J. Chem. Phys.* **143**, 124708 (2015). doi:10.1063/1.4931669 Medline

14. L. Schlapbach, A. Züttel, Hydrogen-storage materials for mobile applications. *Nature* **414**, 353–358 (2001). doi:10.1038/35104634 Medline

15. L. Hornekaer, A. Baurichter, V. V. Petrunin, D. Field, A. C. Luntz, Importance of surface morphology in interstellar H_2 formation. *Science* **302**, 1943–1946 (2003). doi:10.1126/science.1090820 Medline

16. R. Balog, B. Jørgensen, L. Nilsson, M. Andersen, E. Rienks, M. Bianchi, M. Fanetti, E. Laegsgaard, A. Baraldi, S. Lizzit, Z. Sljivancanin, F. Besenbacher, B. Hammer, T. G. Pedersen, P. Hofmann, L. Hornekaer, Bandgap opening in graphene induced by patterned hydrogen adsorption. *Nat. Mater.* **9**, 315–319 (2010). doi:10.1038/nmat2710 Medline

17. M. E. Fornace, J. Lee, K. Miyamoto, F. R. Manby, T. F. Miller 3rd, Embedded mean-field theory. *J. Chem. Theory Comput.* **11**, 568–580 (2015). doi:10.1021/ct5011032 Medline

18. F. Ding, F. R. Manby, T. F. Miller 3rd, Embedded mean-field theory with block-orthogonalized partitioning. *J. Chem. Theory Comput.* **13**, 1605–1615 (2017). doi:10.1021/acs.jctc.6b01065 Medline

19. F. Ding, T. Tsuchiya, F. R. Manby, T. F. Miller 3rd, Linear-response time-dependent embedded mean-field theory. *J. Chem. Theory Comput.* **13**, 4216–4227 (2017). doi:10.1021/acs.jctc.7b00666 Medline

20. D. W. Brenner, O. A. Shenderova, J. A. Harrison, S. J. Stuart, B. Ni, S. B. Sinnott, A second-generation reactive empirical bond order (REBO) potential energy expression for hydrocarbons. *J. Phys. Condens. Matter* **14**, 783–802 (2002). doi:10.1088/0953-8984/14/4/312

21. H. Kim, T. Balgar, E. Hasselbrink, Is there sp^3-bound H on epitaxial graphene? Evidence for adsorption on both sides of the sheet. *Chem. Phys. Lett.* **546**, 12 (2012). doi:10.1016/j.cplett.2012.07.049

22. L. Hornekaer, E. Rauls, W. Xu, Z. Sljivancanin, R. Otero, I. Stensgaard, E. Laegsgaard, B. Hammer, F. Besenbacher, Clustering of chemisorbed H(D) atoms on the graphite (0001) surface due to preferential sticking. *Phys. Rev. Lett.* **97**, 186102 (2006). doi:10.1103/PhysRevLett.97.186102 Medline

23. I. Hamada, M. Otani, Comparative van der Waals density-functional study of graphene on metal surfaces. *Phys. Rev. B* **82**, 153412 (2010). doi:10.1103/PhysRevB.82.153412

24. Y. Wang, H. J. Qian, K. Morokuma, S. Irle, Coupled cluster and density functional theory calculations of atomic hydrogen chemisorption on pyrene and coronene as model systems for graphene hydrogenation. *J. Phys. Chem. A* **116**, 7154–7160 (2012). doi:10.1021/jp3023666 Medline

25. S. Casolo, O. M. Løvvik, R. Martinazzo, G. F. Tantardini, Understanding adsorption of hydrogen atoms on graphene. *J. Chem. Phys.* **130**, 054704 (2009). doi:10.1063/1.3072333 Medline

26. S. Habershon, D. E. Manolopoulos, T. E. Markland, T. F. Miller III, *Ann. Rev. Phys. Chem.* **64**, 387–413 (2013).

27. R. Welsch, K. Song, Q. Shi, S. C. Althorpe, T. F. Miller 3rd, Non-equilibrium dynamics from RPMD and CMD. *J. Chem. Phys.* **145**, 204118 (2016). doi:10.1063/1.4967958 Medline

28. M. Bonfanti, B. Jackson, K. H. Hughes, I. Burghardt, R. Martinazzo, Quantum dynamics of hydrogen atoms on graphene. II. Sticking. *J. Chem. Phys.* **143**, 124704 (2015). doi:10.1063/1.4931117 Medline

29. S. V. Dmitriev, J. A. Baimova, A. V. Savin, Y. S. Kivshar, Ultimate strength, ripples, sound velocities, and density of phonon states of strained graphene. *Comput. Mater. Sci.* **53**, 194–203 (2012). doi:10.1016/j.commatsci.2011.08.019

30. J. Kerwin, B. Jackson, The sticking of H and D atoms on a graphite (0001) surface: The effects of coverage and energy dissipation. *J. Chem. Phys.* **128**, 084702 (2008). doi:10.1063/1.2868771 Medline

31. S. Cazaux, S. Morisset, M. Spaans, A. Allouche, When sticking influences H_2 formation. *Astron. Astrophys.* **535**, A27 (2011). doi:10.1051/0004-6361/201117220

32. F. Karlický, B. Lepetit, D. Lemoine, Quantum modelling of hydrogen chemisorption on graphene and graphite. *J. Chem. Phys.* **140**, 124702 (2014). doi:10.1063/1.4867995 Medline

33. S. Morisset, Y. Ferro, A. Allouche, Study of the sticking of a hydrogen atom on a graphite surface using a mixed classical-quantum dynamics method. *J. Chem. Phys.* **133**, 044508 (2010). doi:10.1063/1.3463001 Medline

34. S. Sakong, P. Kratzer, Isotopic effect on the vibrational lifetime of the carbon-deuterium stretch excitation on graphene. *J. Chem. Phys.* **135**, 114506 (2011). doi:10.1063/1.3637040 Medline

35. S. Sakong, P. Kratzer, Hydrogen vibrational modes on graphene and relaxation of the C-H stretch excitation from first-principles calculations. *J. Chem. Phys.* **133**, 054505 (2010). doi:10.1063/1.3474806 Medline

36. O. Bünermann, H. Jiang, Y. Dorenkamp, D. J. Auerbach, A. M. Wodtke, An ultrahigh vacuum apparatus for H atom scattering from surfaces. *Rev. Sci. Instrum.* **89**, 094101 (2018). doi:10.1063/1.5047674 Medline

37. M. Svensson, S. Humbel, R. D. J. Froese, T. Matsubara, S. Sieber, K. Morokuma, ONIOM: A multilayered integrated MO+MM method for geometry optimizations and single point energy predictions. A test for Diels-Alder reactions and Pt(P(t-Bu)(3))(2)+H-2 oxidative addition. *J. Phys. Chem.* **100**, 19357–19363 (1996). doi:10.1021/jp962071j

38. D. W. Brenner, The art and science of an analytic potential. *Phys. Status Solidi, B Basic Res.* **217**, 23–40 (2000). doi:10.1002/(SICI)1521-3951(200001)217:1<23:AID-PSSB23>3.0.CO;2-N

39. G. C. Abell, Empirical chemical pseudopotential theory of molecular and metallic bonding. *Phys. Rev. B Condens. Matter* **31**, 6184–6196 (1985). doi:10.1103/PhysRevB.31.6184 Medline

40. J. Tersoff, New empirical approach for the structure and energy of covalent systems. *Phys. Rev. B Condens. Matter* **37**, 6991–7000 (1988). doi:10.1103/PhysRevB.37.6991 Medline

41. A. D. Becke, Density-functional thermochemistry. 3. The role of exact exchange. *J. Chem. Phys.* **98**, 5648–5652 (1993). doi:10.1063/1.464913

42. C. Lee, W. Yang, R. G. Parr, Development of the Colle-Salvetti correlation-energy formula into a functional of the electron density. *Phys. Rev. B Condens. Matter* **37**, 785–789 (1988). doi:10.1103/PhysRevB.37.785 Medline

43. S. H. Vosko, L. Wilk, M. Nusair, Accurate spin-dependent electron liquid correlation energies for local spin-density calculations—A critical analysis. *Can. J. Phys.* **58**, 1200–1211 (1980). doi:10.1139/p80-159

44. P. J. Stephens, F. J. Devlin, C. F. Chabalowski, M. J. Frisch, Ab-initio calculation of vibrational absorption and circular-dichroism spectra using density-functional force-fields. *J. Phys. Chem.* **98**, 11623–11627 (1994). doi:10.1021/j100096a001

45. T. H. Dunning Jr., Gaussian-basis sets for use in correlated molecular calculations. 1. The atoms boron through neon and hydrogen. *J. Chem. Phys.* **90**, 1007–1023 (1989). doi:10.1063/1.456153

46. J. P. Perdew, K. Burke, M. Ernzerhof, Generalized gradient approximation made simple. *Phys. Rev. Lett.* **77**, 3865–3868 (1996). doi:10.1103/PhysRevLett.77.3865 Medline

47. S. Grimme, Semiempirical GGA-type density functional constructed with a long-range dispersion correction. *J. Comput. Chem.* **27**, 1787–1799 (2006). doi:10.1002/jcc.20495 Medline

48. P. Hohenberg, W. Kohn, Inhomogeneous electron gas. *Phys. Rev. B* **136**, B864 (1964). doi:10.1103/PhysRev.136.B864

49. W. J. Hehre, R. F. Stewart, J. A. Pople, Self-consistent molecular-orbital methods. I. Use of gaussian expansions of slater-type atomic orbitals. *J. Chem. Phys.* **51**, 2657–2664 (1969). doi:10.1063/1.1672392

50. F. R. Manby, T. F. Miller, P. Bygrave, F. Ding, T. Dresselhaus, F. A. Batista-Romero, A. Buccheri, C. Bungey, S. J. R. Lee, R. Meli, K. Miyamoto, C. Steinmann, T. Tsuchiya, M. Welborn, T. Wiles, Z. Williams, entos: A quantum molecular simulation package. *ChemRxiv* 10.26434/chemrxiv.7762646 (2019). 10.26434/chemrxiv.7762646

51. G. Kresse, Ab-initio molecular-dynamics for liquid-metals. *J. Non-Cryst. Solids* **192–193**, 222–229 (1995). doi:10.1016/0022-3093(95)00355-X

52. G. Kresse, J. Hafner, Ab initio molecular-dynamics simulation of the liquid-metal-amorphous-semiconductor transition in germanium. *Phys. Rev. B Condens. Matter* **49**, 14251–14269 (1994). doi:10.1103/PhysRevB.49.14251 Medline

53. G. Kresse, J. Furthmuller, Efficiency of ab-initio total energy calculations for metals and semiconductors using a plane-wave basis set. *Comput. Mater. Sci.* **6**, 15–50 (1996). doi:10.1016/0927-0256(96)00008-0

54. G. Kresse, J. Furthmüller, Efficient iterative schemes for ab initio total-energy calculations using a plane-wave basis set. *Phys. Rev. B Condens. Matter* **54**, 11169–11186 (1996). doi:10.1103/PhysRevB.54.11169 Medline

55. P. E. Blöchl, Projector augmented-wave method. *Phys. Rev. B Condens. Matter* **50**, 17953–17979 (1994). doi:10.1103/PhysRevB.50.17953 Medline

56. R. Polly, H. J. Werner, F. R. Manby, P. J. Knowles, Fast Hartree-Fock theory using local density fitting approximations. *Mol. Phys.* **102**, 2311–2321 (2004). doi:10.1080/00268970420002748O1

57. F. Weigend, A fully direct RI-HF algorithm: Implementation, optimised auxiliary basis sets, demonstration of accuracy and efficiency. *Phys. Chem. Chem. Phys.* **4**, 4285–4291 (2002). doi:10.1039/b204199p

58. H. Shin, S. Kang, J. Koo, H. Lee, J. Kim, Y. Kwon, Cohesion energetics of carbon allotropes: Quantum Monte Carlo study. *J. Chem. Phys.* **140**, 114702 (2014). doi:10.1063/1.4867544 Medline

59. B. I. Dunlap, J. C. Boettger, Local-density-functional study of the fullerenes, graphene and graphite. *J. Phys. At. Mol. Opt. Phys.* **29**, 4907–4913 (1996). doi:10.1088/0953-4075/29/21/004

60. I. R. Craig, D. E. Manolopoulos, Quantum statistics and classical mechanics: Real time correlation functions from ring polymer molecular dynamics. *J. Chem. Phys.* **121**, 3368–3373 (2004). doi:10.1063/1.1777575 Medline

61. M. Ceriotti, M. Parrinello, T. E. Markland, D. E. Manolopoulos, Efficient stochastic thermostatting of path integral molecular dynamics. *J. Chem. Phys.* **133**, 124104 (2010). doi:10.1063/1.3489925 Medline

62. M. Andersen, L. Hornekaer, B. Hammer, Graphene on metal surfaces and its hydrogen adsorption: A meta-GGA functional study. *Phys. Rev. B* **86**, 085405 (2012). doi:10.1103/PhysRevB.86.085405

63. Y. J. Dorenkamp, thesis, Georg-August Universtiy of Goettingen (2018).

64. H. C. Andersen, Molecular dynamics simulations at constant pressure and/or temperature. *J. Chem. Phys.* **72**, 2384–2393 (1980). doi:10.1063/1.439486

65. E. Bitzek, P. Koskinen, F. Gähler, M. Moseler, P. Gumbsch, Structural relaxation made simple. *Phys. Rev. Lett.* **97**, 170201 (2006). doi:10.1103/PhysRevLett.97.170201 Medline